E-ISSN: 2583-9667
Indexed Journal
Peer Reviewed Journal
https://multiresearchjournal.theviews.in

Received: 16-10-2025
Accepted: 22-11-2025
Published: 18-01-2026

INTERNATIONAL JOURNAL OF ADVANCE RESEARCH IN MULTIDISCIPLINARY

Volume 4; Issue 1; 2026; Page No. 310-325

Magnetic Nanoparticle-Based Biosensing for Rapid and Sensitive Detection of Biomolecular Targets in Biomedical Applications

[1]Kasula Rajya Laxmi and [2]Dr. Vipin Kumar

[1]Research Scholar, Department of Physics, Monad University, Hapur, Uttar Pradesh, India
[2]Professor, Department of Physics, Monad University, Hapur, Uttar Pradesh, India

DOI: https://doi.org/10.5281/zenodo.21900527

Corresponding Author: Kasula Rajya Laxmi

Abstract

Magnetic nanoparticles (MNPs) have emerged as promising materials for advanced biomedical biosensing because of their distinctive magnetic properties, high surface-to-volume ratio, and ability to interact selectively with biological targets. This study proposes the development of a magnetic nanoparticle-based biosensing system for rapid and sensitive detection of biomolecular targets in biomedical samples. The proposed approach investigates the interaction of functionalized MNPs with target biological agents and utilizes their magnetic response for quantitative detection. A magneto-resistive, particularly Giant Magnetoresistance (GMR)-based, sensing platform is considered for measuring changes in magnetic field generated by the concentration and distribution of MNPs associated with target analytes. The research focuses on the design and optimization of the sensing architecture, signal-conditioning and processing circuits, nanoparticle functionalization, and quantitative analysis of sensor responses. Important performance parameters, including sensitivity, selectivity, limit of detection, response time, repeatability, and measurement accuracy, will be evaluated under controlled experimental conditions. The proposed system aims to provide a compact, rapid, reliable, and potentially low-cost alternative to conventional laboratory-based detection techniques. The study further investigates the influence of nanoparticle size, concentration, surface modification, and magnetic properties on biosensor performance. The expected outcome is an integrated nanoparticle-based magnetic biosensing platform capable of detecting and quantifying selected biological or biomolecular agents in liquid samples. Such a system could contribute to the development of portable point-of-care diagnostic technologies and facilitate rapid biomedical screening. The research is expected to strengthen the application of nanotechnology, magneto resistive sensing, and signal processing in next-generation biomedical diagnostics.

Keywords: Magnetic Nanoparticles, GMR Sensor, Magneto-resistive Biosensing, Biosensor, Biomolecular Detection, Nanotechnology, Biomedical Diagnostics, Signal Processing, Point-of-Care Detection, Magnetic Sensing

1. Introduction

Nanotechnology is a multi-faceted division that deals with synthesis, strategizing and maneuvering of particles to nano-size (below 100 nm) range. Its application in medicine is a speedily developing area of investigation. Numerous strategies are solicited to synthesize materials at nanoscale. Inorganic (metal) Nps can be considered as a resourceful classification of nanoparticles because of their implementation in physics, electronics, chemistry, medical, and pharmaceutical applications. Amidst, the gold nanoparticles stick out in dominance because of its assets like; attuned optical properties, stable, non-toxic, biocompatible, and effortlessly changing surface chemistry. Due to unique physical–chemical characteristics, AuNPs are extensively used as conveyor of antibiotics/drugs & small molecules to revamp prognosis and therapeutics of cancer and targeting antibiotic resistance, along with its use in bioimaging and real time monitoring of drug response. Gold is a quintessential, unreactive element, and is known for its long-lasting luster without getting oxidized. Not only in its elemental form, but gold in its nano range is highly preferred in biomedical applications. Gold nanoparticles enter/accumulate at the cancerous/inflammation sites much more swiftly, when compared to other molecules. Their usage in bio diagnostics or as artificial antibodies (as the binding affinity with ligands can be accurately modulated) is in demand due to the intense photophysical properties exhibited by them. The antibacterial efficacy of gold nanoparticles in various nano-morphologies (rods, flowers, stars, spheres, and capsules) synthesized using green

approach (discussed below), by utilizing phytochemicals as reducing and stabilizing agents, have been analyzed. Since it possesses multivalency, it can bind to many types of ligands present on both Gram-positive and Gram-negative bacteria. AuNps can be considered as nano-bullets against threatening antibiotic resistance rapidly observed in bacteria. Synthesizing them in smaller sizes allows formation of irreversible pores while translocating into the microbial cell membrane, along with scrupulously unsettling and altering the cellular pathways serving as an intrinsic drug agent. All the above discussed assistance of gold nanostructures in biomedical applications can be tailored to come up with an efficient diagnostic, targeting and therapeutic nano agent. In this study anticancer and antibacterial potency of AuNps synthesized from *Citrus maxima* plant has been taken forward.

Advent of multi-drug resistant infectious microorganisms stipulates execution of novel antimicrobials. According to the World Health Organization (WHO) report, antimicrobial resistance (AMR) is a foremost worldwide threat to public health. Considering the economic loss due to AMR, annual health expenses and production losses in the European Union alone, was estimated to be ~2.5 million hospital days, 25,000 deceases and an economic burden of nearly~€1.5 billion. Bacteria like multi-drug resistant MDR-*Pseudomonas aeruginosa* causes infections in burns, cystic fibrosis, traumas, cancer, chronic obstructive pulmonary disease (COPD), sepsis, and ventilator-associated pneumonia (VAP) including those caused by COVID-19. It has antibiotic evasion mechanisms, causing antibiotic resistance. Hence, scientists across the world are significantly interested in developing novel strategies to fight AMR. Thus, here the age-old antimicrobial tactics of gold is exemplified synthesizing through fruit, peel and leaf extracts of *C. maxima* plant.

Cancer ravages ~10 million lives every year in spite of great advances in medicine and technology. Also, a destructive tumor lies inactive for a long time and later emerges/re-emerges, leading to enormous suffering in patients, and demand for aggressive therapeutics. Chemo and radiation therapies result in several adjacent side effects (hair loss, bone marrow suppression, and gastrointestinal issues) due to injury of nearby healthy tissues, along with emergence of resistance against given therapies. Considering cancer as a dynamic and the second major cause of deaths, there is a dire requirement of novel therapies that displays solutions for drug resistance and is targeted towards cancer cells, instead of normal cells. Various types of AuNPs such as nanorods, cages, stars, cubes, and spheres, have been considered as effective and biocompatible tools for their plausible role in cancer treatment.

AuNPs synthesis via physical and chemical course is thus-far secured. But, these methods in general apply toxic materials and non-polar solvents, that cause perilous bearings to the environment and entails several steps for purifying products, ensuing in an expensive process. In such lines, biosynthesis is an environmentally safe method having ascendancy over conventional approaches. Green synthesis from plants, fungi, bacteria, and algae is forerunner for gold ion reduction by acting as natural reducing, stabilizing and capping agents to synthesize nanoparticles with desired morphology and size remarkable for nanoscience. Biosynthesis is observed as a low-cost, simple, and environmentally-safe method, because of its use of non-toxic solvents, like water. Though, synthesis by plant extracts, imparts better platform because of their natural and non-toxic phytochemical agents along with curtailing the expenses of microbe isolation and proliferation. Plant extracts are multifaceted combinations delivering affluent armory of molecules with high oxido-reduction, like; amino acids, flavanones, aldehydes, fatty acids, flavones, terpenoids, flavonoids, chalcones, and alcohols. Additionally, biosynthesis churns out profuse, thoroughly stable Nps with better-defined size than conventional methods since there is involvement of phytochemicals as reducing and stabilizing agents. It raises high yield, and is less time consuming, biocompatible. Also, the size of nanoparticles can be supervised by monitoring parameters like, temperature, stirring speed, pH and concentration of reactants. Hence, this study is done to explore the antioxidant, anti-microbial and anti-cancer potential of AuNps made up of extracts of *Citrus maxima* (Pomelo) plant. Extracts of fruit, peel, and leaf of *C. maxima* plant were used as green source of precursors in order to biosynthesize gold nanoparticles due to its pharmacological activities conceived because of phytochemicals. It is a perennial plant having edible fruits with innumerable medicinal values like antioxidant, anticancer, and antibacterial properties.

Citrus family is known for its antioxidant potential. *C. maxima* is a major source of Vitamin C, flavonoids (hesperidin, neohesperidine dihydrochalone), and polyphenols, which acts as antioxidants and hence neutralizes free radicals, thus avoiding oxidative damage. It was tested in *C. maxima* fruit juice treated rats and its shielding part against H_2O_2, Streptozotocin, and Nitric oxide generating system was investigated. Here induced DNA damage was seen which might be due to individual or synergistic action of various active principles involved in a diverse range of biological processes against oxidative stress. Peels exhibit higher antioxidant content and potential than their pulps as it is a rich source of natural antioxidants, in order to protect the fruit from getting oxidized. Antibacterial activities of the phytochemical constituents of the pericarp, mesocarp and segment membrane crude ethanolic, methanolic and water extracts of *C. maxima* fruit, and leaves were tested against *E. coli* and *Salmonella typhimurium*, *P. aeruginosa*, *Klebsiella pneumoniae*. Citrus peels have also shown antibacterial efficiency against pathogenic microbes like *E. faecalis* and *P. putida*. Not only antibacterial but the potential of *C. maxima* extracts has been exploited for anticancer potential. Limonoids (limonin and nomilin) have chemo defensive properties, free radical-scavenging, and glutathione S-transferase-inciting activity. *C. maxima* peel has apoptosis inducing properties by blocking S phase of the cell cycle and down regulating the Bcl-2 and up-regulating Bax concentrations. This can be credited to immunoregulatory action of polysaccharides and apoptosis inducing behavior in the tumor-bearing mice. Fruit juice of this plant contains 1,1-diphenyl-2-picrylhydrazyl (DPPH), lycopene, and β-carotene, known to possess antioxidant potential, and better anti-proliferative capability in leukemia cells. *C. maxima* MeOH leaf extract increased non-viable cancer cell count, the life span, and

reduction in tumor volume in Ehrlich's Ascites carcinoma cell (EAC)-treated mice. Presence of flavonoids and limnoids in *C. maxima* can be the probable agents for exhibiting anticancer effects.

2. Materials and Methods

2.1 Biosynthesis of silver nanoparticles using *C. maxima* extracts

Plant extract preparation was executed, as designated previously. Fruit, leaves and peel of *C. maxima* plant were collected and cleaned with sterile water. Fruit extract was made by filtering fruit juice by sterile Whatmann filter. 10 gm of dried, crushed leaves and peel were suspended in 100 ml of MilliQ water and heated in oil bath at 80 °C for 2 hr in round bottom (RB) flasks and filtered. 20 ml of extracts were added dropwise in RB flask containing 200 ml of 1 mM HAuCl4 solution with constant stirring at room temperature. The color of the solution changed from colorless to purple brown within 4–6 h. Gold nanoparticles were harvested through high-speed centrifugation followed by water washing and lyophilization.

2.2 Characterization of biosynthesized nanoparticles

AuNps biosynthesis was confirmed by analyzing the spectra (200–800 nm) using UV–Vis spectrophotometer. Homogeneous aqueous solutions of AuNps (1 mg/ml) were used for Dynamic Light Scattering (DLS) measurement using Zetasizer Nano-ZS (Malvern Inc, UK). Fourier Transform Infrared (FTIR) spectra were recorded using a single-beam Spectrum RXI-MID-IR (PerkinElmer, USA), (scan parameters: scan range: 4400–400 cm^{-1}; number of scans: 16; resolution: 4 cm^{-1}; interval: 1 cm^{-1}; unit % T). Shape and size of AuNps were investigated using Transmission Electron Microscopy (TEM: voltage of 200 kV (Tecnai G2 30 U-twin, 300 kV Ultra-twin microscope).

2.3 Antioxidant activity

The antioxidant activity of AuNps was done following the DPPH quenching method. Briefly, *C. maxima* extracts and AuNps were diluted in the range of 100-1000 µg/ml. 100 µl of dilutions were mixed with 100 µl of 2, 2-diphenyl-1-picrylhydrazyl solution (80 µg/ml, DPPH, HiMedia) in a 96-well plate (Corning) and incubated in dark for 30 min at room temperature. Quercetin and methanol were used as positive and negative controls, respectively. The DPPH free-radical scavenging activity (%) was analyzed after taking absorbance at 517 nm using Tecan microplate reader.

2.4 Antimicrobial activity

The antimicrobial activity of AuNps was verified against pathogenic microbes: *Pseudomonas aeruginosa* (MTCC 741), *Bacillus cereus* (MTCC 430), multi-drug resistant *Pseudomonas aeruginosa* (ATCC 27853). These were cultured in Brain Heart Infusion broth and agar (HiMedia) at 37 °C. Gentamicin (0.01 mg/ml) (HiMedia) and sterile water were used as positive and negative controls, respectively. Fresh culture of absorbance 0.5 (600 nm) was prepared in BHI broth. Antimicrobial activity was detected by Kirby-Bauer disk diffusion assay. Mueller Hinton agar plates were spread with bacteria, over which sterile discs of 6 mm were placed and soaked with 50 µl of *C. maxima* extracts (1 mg/ml), HAuCl4 (1 mM), Gentamicin and sterile water, followed by overnight incubation at 37°C. The growth inhibition was checked by measuring zone of inhibition (mm) formed around each disc (Antibiotic zone scale, HiMedia). Minimum inhibitory concentration (MIC) of AuNps against pathogens was assessed by microbroth dilution method done in 96-well plates. Media with inoculum served as growth controls. Absorbance was taken at three-hour intervals till 12 hours using the TECAN spectrophotometer at 600 nm, to analyze growth kinetics. Then, 50 µl (200 µg/ml) of p-iodonitrotetrazolium chloride (HiMedia) was mixed into wells and incubated at 37 °C for 30 min to screen the colour change from colour less (no growth) to pink (growth). Experiment was done in triplicates.

2.4.1 Colony-Forming Unit (CFU) Assay

Single colony of MDR- *Pseudomonas aeruginosa* (MDR-PA) was inoculated in 5 mL of sterile Mueller Hinton broth and incubated at 37 °C and 180 rpm, until absorbance of 0.5 OD at 600 nm reached. Minimum inhibitory concentration (MIC) assay in a 96-well plate was set with AuNps, with a final volume of 200 µL with 10 µL as volume of inoculum used. PBS-treated wells with inoculum served as the negative control. Absorbance pre and post incubation of 12 h was taken at 600 nm in a TECAN microplate reader. Later, the entire well volume was taken and serially diluted till 10^{-9} in eppendorfs with 900 µL of fresh media. Dilution of 10^{-6} was plated in Mueller Hinton agar plates and incubated overnight and 180 rpm. Post overnight incubation at 37 °C, the colonies were counted and total CFU was calculated.

2.5 Mechanism of action of antimicrobial activity displayed by AuNps

2.5.1 Transmission Electron Microscopy (TEM)

Fresh culture of MDR- PA untreated and treated with AuFeNps at its MIC and was incubated for 1 hr at 37 °C. Cells were later centrifuged at 3000 rpm for 10 min. The untreated bacteria served as control. The pellet was washed with 1X PBS (pH 7.4) and fixed with 4% paraformaldehyde (Sigma) at 4 °C overnight. Dehydration of samples was done by washing with an ascending concentration of ethanol (10–100%). Pellets were resuspended in 200 µl of sterile water followed by staining with 1% uranyl acetate (Hi Media) for 5 min. 10 µl of these cells were loaded on carbon-coated TEM grids (200 mesh Cu, TED Pella Inc., USA), air dried and imaging was done.

2.5.2 Cell membrane permeability of MDR-*Pseudomonas aeruginosa* by AuNps

The cell (MDR-PA) survival capability of AuNps was analyzed using Resazurin dye. This dye reflects cell survival ability by changing colour from blue (non-fluorescent) to pink (highly fluorescent). Colour change occurs due to chemical reduction of resazurin to resorufin, consequential of aerobic respiration (if the cells are live). Cultures of MDR- PA of OD600nm = 0.5, were used in this experiment. AuFeNps, AuPeNps, AuLeNps at their respective MIC were diluted in Mueller Hinton Broth and added in 96 well plates along with 10 µl of bacteria. Post overnight incubation of this plate at 37 °C, to each well 20 µl of resazurin was added and incubated at 37 °C for 30 min, subsequently

fluorescence was read at an excitation λ=530 nm and emission λ= 90 nm in a multimode microplate reader (TECAN).

2.5.3 Cell Membrane damage

To evaluate the membrane leakage in MDR- PA by AuNps, 10^8 cells were treated with AuNps at the MIC, and incubated at 37 ºC for 6 h. Cells treated with PBS served as negative control. Post incubation, cells were washed twice with 1X PBS and resuspended in 500 µL of PBS having 10 µM Propidium iodide (PI) to detect the membrane leakage. Fluorescence was measured at excitation, 535 nm; emission, 617 nm in a multimode plate reader (TECAN).

2.5.4 Reactive oxygen species detection

MDR-*Pseudomonas aeruginosa* cells were treated with various AuNps for 4 h and 3% H2O2 (positive control) for 30 min, whereas untreated cells served as negative control. Cells were washed two times with 1X PBS and incubated with 5 µM 2',7'-dichlorodihydrofluorescein diacetate (H2DCFDA; Sigma-Aldrich) at 37 ºC for 30 min. ROS production was measured 488 nm excitation and 520 nm emission by a multimode microplate reader (TECAN).

2.5.5 Protein leakage

To comprehend if AuNp treatment in MDR-PA is leading to cytosolic protein leakage, cells were treated with AuNps at the MIC and incubated for 6 h at 37 ºC (182). Later, cells were spinned at 12,000 RPM for 10 min. 2 µl of supernatant was used to estimate the protein content using Bradford protein assay reagent (Bio-Rad) and incubated in dark at 37 ºC for 30 min. Bovine serum albumin was used for standard curves. Absorbance at 595 nm was measured by the TECAN plate reader.

2.5.6 DNA Damage with AuNp treatment

Genomic DNA damage in MDR- PA was evaluated associated with AuNp treatment. MDR- PA was exposed to the MIC of AuNps for 4 h to find if AuNp is inducing apoptosis in bacteria. Cells were then washed with 1X PBS and genomic DNA was isolated using Qiagen DNA isolation kit. Concentration of DNA was estimated using the Nanodrop spectrophotometer. DNA damage was analyzed in an agarose gel electrophoresis and imaged by Gel Doc system (Bio-Rad).

2.6 Anti-cancer potential

Breast cancer cell line luminal (MCF7) and myoepithelial or basal type (MDA-MB-231), Human fibrosarcoma (HT-1080) and mouse melanoma (B16-F10) cell lines were used. HT-1080, MCF-7 cells were grown in DMEM- High glucose medium (Sigma), and B16-F10 cell lines were maintained in DMEM-F12 medium, whereas MDA-MB-231 was maintained in RPMI, along with 10% Fetal Bovine Serum (Gibco) in a humidified 5% CO_2 incubator at 37 °C.

2.6.1 Metabolic activity of the cells

In order to determine cell viability of the cell lines on treatment with nanoparticles, Cell Titer-Glo assay kit (Promega) was used following the standard protocol. 1×10^4 cells/well was seeded in Nunc 96 well plates. Wells were treated with nanoparticles (10–250 µg/ml of AuFeNps, AuLeNps, AuPeNps) and *C. maxima* plant extracts and incubated for 48 hr. Untreated cells were used as control. Substrate was used for generating luminescence (Cell Titer Glo (Promega)) and it was recorded in the TECAN plate reader. Experiments were performed in triplicates.

2.6.2 Cytotoxicity of cancer cells

MTT assay was also performed to identify the toxicity of AuNps on the above cell lines. 10^4 cells/well in 100 µL of DMEM-F12 with 10% fetal bovine serum (FBS) culture medium were plated in a 96-well plate and incubated in 5% CO_2 at 37 °C. Then, entire wells were decanted and washed with 1X PBS, followed by adding 100 µL of MTT reagent (1 mg/mL in PBS) and incubating for 2 h. The purple formazan crystals formed were dissolved in 100 µL of DMSO. The absorbance was measured at 540 nm and a reference wavelength of 620 nm. Percentage viable cells were analyzed in view of untreated cells as 100% viable.

2.6.3 Scratch-induced migration assay

Migration of breast cancer cells (MCF-7) was demonstrated using an *in vitro* scratch method as described by Liang et al. with minor modifications. 12-Well plate (Nunc) was used for seeding cells and post achieving monolayer confluency, a linear scratch was applied using a 10 µl pipette tip. This scratch was photographed by an inverted phase-contrast microscope with a digital camera (Leica Microsystems GmbH, Solms, Germany), along with marking of the exact location on the plate. Treatment in these wells was done with 40 ug/ml of AuFeNp and incubated at 37 ºC with 5% CO_2. Scratch injury was again photographed post 24 hour of incubation, to assess the total wound closure by determining the area between the edge of the injury (before and after treatment). Results were analyzed using ImageJ Fiji software and expressed in % reduction in injury closure distance, considering the untreated cells representing 100%.

2.6.4 Intracellular ROS generation in breast cancer cell lines

Intracellular reactive oxygen species (ROS) generated by the AuNps were detected by the 2′, 7′-dichlorodihydrofluorescein diacetate (H2DCFDA) (Sigma-Aldrich). MCF-7, MDA-MB231 and B16-F10 cells were cultured in 96-well plates to nearly 80% confluency. Wells were treated with 10 mM H2DCFDA and incubated for 45 min at 37 °C. Post PBS wash, wells were treated with AuNps at their respective IC50. The fluorescence was measured at 488 nm excitation and 520 nm emission by a multimode microplate reader (TECAN) to analyze intracellular ROS levels.

2.6.5 Characterization of toxicity of AuNps on B16-F10 cell line

Morphological evidence for the detection of apoptosis in B16-F10 cell line, treated with AuFeNps, was carried out using Acridine orange and Ethidium bromide (HiMedia) dual dye staining. The B16-F10 cell line was treated with AuFeNps (10 µg/ml), fruit extracts (50 µg/ml) and HAuCl4 followed by incubation for 48 h. Cells were harvested, centrifuged at 1500 rpm for 10 min at 4 °C, washed thrice and resuspended in 1X PBS (pH 7.4). 10 µg/ml of acridine orange (AO) and 10 µg/ml of ethidium bromide (EtBr) in

1X PBS were mixed to prepare AO/EtBr mix. Cell suspension was stained with AO/EtBr mix and observed under fluorescence microscope (Zeiss) using fluorescein filter. Cell viability of the B16-F10 cell line was assessed using trypan blue. DNA fragmentation assay was done to observe fragmentation of DNA that occurs during apoptosis due to the activation of caspase-3. Whole genomic DNA from treated B16-F10 cell line was isolated using DNeasy blood and tissue kit (QIAGEN) and analyzed on 1% agarose gel in order to scrutinize the internucleosomal DNA laddering in the treated cells.

2.6.6 Cell cycle analysis using fluorescence-activated cell sorting (FACS)

Cell cycle analysis using flow cytometry (BD Biosciences) was performed for the nanoparticles treated with B16-F10 cells. Treatment and harvesting of B16-F10 cells were done as defined previously. Pellet was fixed in 200 µl of 70% ethanol at 4 °C for 24 h followed by washing with 1X PBS and centrifugation at 2000 rpm for 5 min. 0.1% Triton X-100 (Sigma) and RNase (40 µg/ml) (HiMedia) were added to the pellet and incubated at 37 °C for 45 min. Cells were stained with 50 µg/ml propidium iodide, incubated for 15 min in dark at room temperature and then the cell cycle was analyzed by flow cytometry (BD FACSAria™III). The number of cells present in each growth phase was analyzed using ModFit software.

2.6.7 Caspase-3 activity assay

Caspase-3 activity was measured in AuNps treated B16-F10 cell line. 1.5×10^5 cells were seeded in a 6-well plate and treated with 10 µg/ml AuNps, 50 µg/ml extract, 1 mM HAuCl4 and untreated cells were used as control. Post incubation of 48 h, Caspase-3 activity was performed using Caspase-Glo® 3/7 Assay (Promega). Cleavage of the fluorogenic substrate was measured in TECAN fluorometer (excitation: 380 nm; emission: 460 nm) and the activity was represented as Relative Fluorescence Units (RFU).

2.7 Cyto-compatibility of AuNps

2.7.1 Cytotoxicity of AuNp

Normal human lung fibroblast (MRC-5), human keratinocytes (HaCaT) were normal cell lines used to identify the toxicity of AuNPs on these cells. MRC-5 was maintained in DMEM whereas, HaCaT was maintained in DMEM-F12 medium, and incubated at 37 ºC with 5% CO_2. Cell Titer-Glo assay kit (Promega) was used to assess the toxicity caused by AuNps on these cells, using the protocol mentioned above in the 2.7.1.

2.7.2 Biocompatibility of nanoparticles in a co-culture model

Next to identify appropriate proliferation of keratinocytes in the presence of AuNps, a coculture of HaCaT and MRSA bacteria was established. 10,000 cells per well were seeded in 96-well plates and incubated until the confluence reached 75-85%. Then, fresh media supplemented with glucose, having bacterial absorbance (600 nm) of 0.1 was added to the confluent HaCaT wells and incubated for 4 h at 37 °C without shaking. This coculture was treated with 40 µg/mL of AuNPs solutions for 12 h. Later, this media along with bacteria was removed and plated on Mueller Hinton Agar to check the bacterial count. And the keratinocytes were washed three times with 1X PBS pH 7.4, and the viability of HaCaT was analyzed by MTT assay as mentioned above.

Later to confirm the appropriate proliferation of keratinocytes in the AuNp system, a coculture of HaCaT and MDR- PA bacteria was established. 10, 000 cells were seeded in a 96-well plate, and 80–90% confluency was maintained for treatment. MDR- PA was grown in DMEM (added glucose) until an OD600nm of 0.1, which was added to confluent HaCaT and incubated at 37 °C for 12 h. Media was removed to get rid of external bacteria and co-culture was treated with 10 µg/ml of AuFeNp for 12 h. Subsequently, media was decanted and cells were washed three times with 1X PBS, and cell proliferation (health) was analyzed by LDH assay (Iodonitrotetrazolium chloride) for cell proliferation according to the manufacturer's protocols. Cell morphology analysis HaCaT cells were seeded on a coverslip kept in 12 well plate (Nunc). Post incubation for 24 hours, cells were treated with AuNps for 24 hours and later washed with 1X PBS and fixed with liquid 2% glutaraldehyde + 2% formaldehyde for 30 min. Samples were washed three times with 1X PBS. Cell nuclei and actin filaments were stained with DAPI (NucBlue Live Ready Probes Reagent, Thermo Fisher Scientific) and Alexa Fluor 488 (ActinGreen 488 ReadyProbes Reagent, Thermo Fisher Scientific) for 30 min, respectively. The coverslips were mounted on slides using Gold Antifade Mountant (Thermo Fisher Scientific) and cells were imaged at various magnification using an inverted fluorescence microscope (Ti-E–V5.30, Nikon, Tokyo, Japan) at phase contrast and with appropriate filter settings (λex = 549 nm; λem = 565 nm for Phalloidin and λex = 330-380 nm; λem = 435–485 nm for DAPI). Images were analyzed using ImageJ software.

2.7.3 Hemolytic activity

It was implemented following the standard protocol. Human red blood cells were washed thrice with 1X PBS, centrifuged at 1500 rpm for 10 min at 4 °C. 100 µl of 4% RBCs was added in each well of 96-well plate, containing 160, 800 and 1600 µg/ml of AuFeNps, AuLeNps, and AuPeNps. 1% Triton X-100 (Sigma) and PBS were positive and negative controls, respectively. Plate was incubated at 37 °C for 1 hr, centrifuged at 2000 rpm for 10 min. 100 µl of supernatant was transferred to a fresh plate and absorbance was recorded at 540 nm using TECAN multimode plate reader. Experiment was done in triplicates.

2.8 Statistical Analysis

All the experiments were performed in three independent experiments and the results were expressed as mean ± standard deviation (Mean ± SD) by using one-way analysis of variance (ANOVA).

3. Results and Discussion

3.1 Green synthesis of gold nanoparticles

Specific proportions of fruit juice, peel and leaf extracts of *C. maxima* plant was used as reducing agent of HAuCl4 (Gold (III) chloride trihydrate) to synthesize AuFeNps, AuPeNps and AuLeNps, respectively, by modifying Turkevich Method of synthesis of nanoparticles. In order to get stable and non-aggregating AuNps, various

concentrations and volumes of extracts were put to reaction. The confirmation of the formation of AuNps was estimated by the colour change of the reaction mixture from light yellow to dark purple (Fig No. 3.1A). This colour change is attributed to the surface plasmon resonance (SPR) displayed by AuNps. Using plant extracts as reducing and stabilizing agents, AuNps were synthesized within 30 min of the reaction, demonstrating a rapid synthesis model for gold nanoparticles.

3.2 Characterization of biosynthetic gold nanoparticles

To standardize the volume of extracts for proper and stable synthesis of AuNps, fruit juice was taken in different volumes (2ml (Fe2), 4 ml (Fe4), and 6 ml (Fe6), and that specific volume, corresponding to the peak obtained using UV–Vis spectroscopy was chosen for further synthesis. Also the colour change from yellow to ruby pink/purplish demonstrated visible formation of AuNps [Fig 3.1 (A)]. Distinct peak between 500-600 nm was obtained in UV-Vis spectroscopy due to the localized surface plasmon resonance exhibited by AuNps [Fig 1(B)]. With increase in the volume of extract the time taken for the synthesis has decreased, also exhibiting a slight peak shift (540 nm for AuFe2Nps to 549 nm for AuFe4Nps and AuFe6Nps). Though, the full-width-half-maximum of AuFe6Np was higher than AuFe2Np and AuFe4Np (not much difference between them). Thus, considering Mie's theory, the size of nanoparticle is inversely proportional to FWHM, hence size of nanoparticles generated by using 6 ml of extract is showing smaller size of AuNps, hence for further synthesis this ratio was used. 1 mg/ml aqueous solution of AuNps, duly sonicated and homogeneously dispersed was used to estimate the diameter (d, nm), polydispersity index (PdI) and zeta potential (mV) measurements using Dynamic Light Scattering (DLS, Malvern Instrument), where the sizes of AuNps ranged between 120 to 250 nm (Table 3.1).

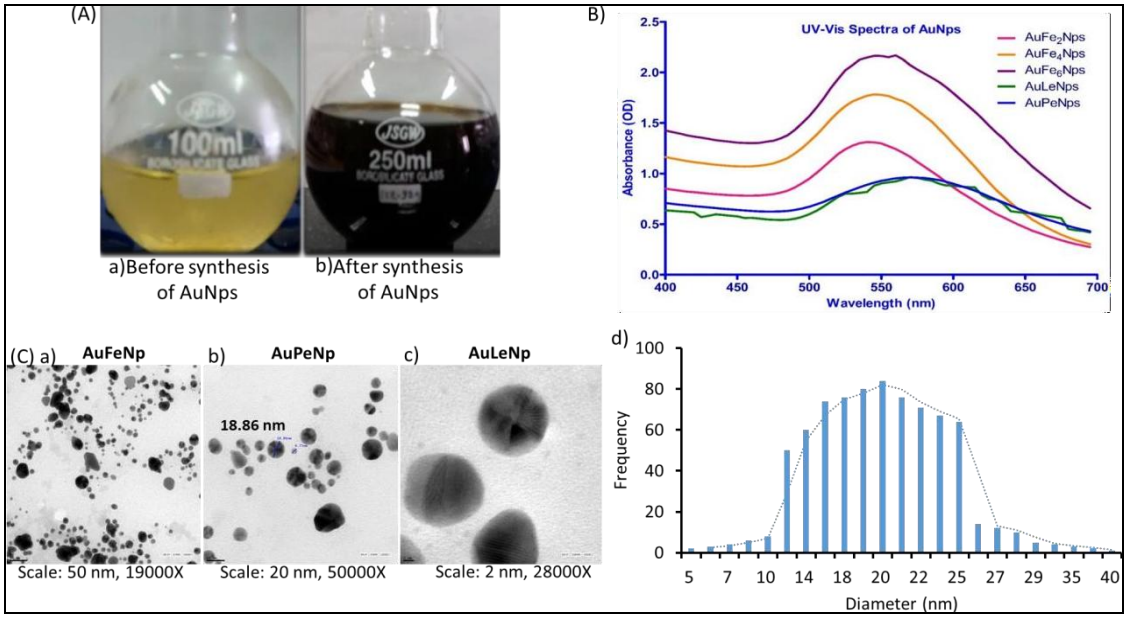

Fig 3.1: Synthesis and characterization of biosynthesized gold nanoparticles (AuNps): A) formation of AuNps represented by change in color before and after the reaction; B) UV–Vis absorbance peaks in the range of 400–700 nm showing peak between 500-600 nm; C) Transmission electron microscopy (TEM) images showing the AuNps D) Frequency distribution of size estimation of AuNps by TEM

Table 3.1: Size, polydispersity index and zeta potential of biosynthesized AuNps

Nanoparticles	Size (d, nm) ± SD	PdI ± SD	Zeta Potential (mV) ± SD
AuFeNp	124 ± 2.7	0.15 ± 0.04	-17.9 ± 0.9
AuPeNp	111 ± 2.5	0.21 ± 0.008	-16.9 ± 0.41
AuLeNp	248 ± 17	0.43 ± 0.01	-11.2 ± 0.26

DLS spots the scattered light intensity variations instigated by the Brownian motion of the nanoparticles in a liquid suspension, revealing both the average size and size distribution of nanoparticles. Using the fluctuations of scattered light intensity, diffusion coefficient and hydrodynamic size of nanoparticles can be estimated using Stokes-Einstein equation. Nanoparticles should also be characterized for their suitability in *in vitro* and *in vivo* applications. Suitability can be characterized by a dimensionless parameter called "polydispersity index" (PDI) or heterogeneity index, which describes the degree of non-uniformity of size distribution of nanoparticles. PdI values smaller than 0.05 observe highly monodisperse levels, whereas values higher than 0.7 corresponds to bigger particle size distribution. PdI of AuNps found in this study (Table No. 3.1) suggest that AuFeNps is highly monodisperse and non-aggregating in aqueous suspension, followed by AuPeNps. But AuLeNps showed little higher PdI (0.43), which can be the reason behind the aggregation of nanoparticles synthesized from the leaf extract. AuFeNps showed negligible aggregation, AuPeNps started to aggregate post a week of dispersion in aqueous solution, whereas AuLeNps aggregated a day post synthesis. The non-aggregation in AuFeNps and slow aggregation in AuPeNps can be attributed to the phytochemical agents present in fruit juice and peel extract which acts as capping agents in order to minimize the uncontrolled aggregation of nanoparticles. Capping agents function by creating electrostatically-induced steric barriers between the synthesized nanoparticles. Capping agents are simply

"binding molecules" that are required in minute concentrations for the biosynthesis of Nps. This modifies the morphology, size distribution, and surface chemistry of Nps along with acting as armor to avoid agglomeration and improve the reduction kinetics of Nps by forming complex structures with metallic ions in the corresponding salts. These capping and stabilizing agents were identified through Fourier Transform Infrared (FTIR) spectroscopy. FTIR established the incidence of various functional groups on AuFeNp which indicated that phytochemicals present in fruit juice got adsorbed on the surface of AuNp synthesized using fruit juice, represented in the Figure and Table 3.2 below.

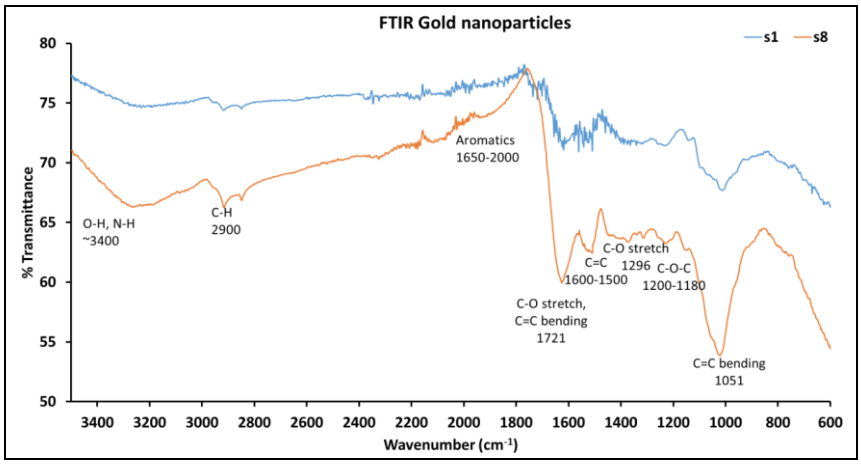

Fig 3.2: Fourier transform infrared spectroscopy (FTIR) data showing the presence of various functional groups in the fruit extract (blue-s1), and AuFeNps (orange-s8).

Table 3.2: Functional groups identified on AuFeNps

Functional Group	Corresponding wavenumber (cm-1)
Aromatics	2000-1650
O-H bend	1419
C-O stretch	1296
C-O stretch, C=C bending	1721
O-H, N-H	3400
C-H and O-H stretch	3000-3100
C=C bending	1051
C-O-C	1200-1180
C=C	1600-1500
C-H	2900

Table 3.2 indicates the negative zeta potential values of AuNps representing the negative charge over them, where AgFeNp is highly negatively charged than AuPeNp and AuLeNp. Nps having zeta potential ranging from −10 to +10 mV represent neutral charge, whereas potential greater than +30 mV or less than −30 mV is strongly cationic and anionic in nature, respectively. Zeta potential is imperative for the stability of nanoparticles in suspension form as the surface charge determines the initial adsorption of Nps on the cell membrane. Post adsorption, the endocytotic uptake rate is affected by the size of Nps. Thus, zeta potential and size of Np determines the toxicity caused by nanoparticles. Size and shape of AuNp was further established by Transmission Electron Microscopy (TEM). It revealed spherical shape of AuNp and size ranged between 5 to 40 nm, where AuFeNp (5-30 nm) and AuPeNp (12-35 nm) were smaller in size than AuLeNp (35-40 nm) (Fig 1(C-D). Size in TEM was lesser than DLS, which might be attributed to the hydration of particles that creates hydrodynamic diameter around the nanoparticles in DLS. Identifying the size of the Nps is imperative with respect to the biological functions post adsorption/internalization in the cell, as it is the size that determines their toxic potential.

3.3 Biosynthetic gold nanoparticles displayed antioxidant potential

C. maxima is a citrus plant hence, it was anticipated that AuNp synthesized from the extracts of this plant would exhibit antioxidant potential due to the richness of antioxidants in extracts. DPPH radical scavenging potential of the extracts and Nps was estimated. The purple colour of the DPPH radical is because of the presence of an odd electron in it, which also allows its absorbance at 517 nm. Thus, when an antioxidant molecule/compound present on the surface of the AuNps donates an electron to DPPH, it loses its purple colour which can be measured quantitatively through changes in the wavelength. Out of the given Nps, AgFeNp displayed highest antioxidant potential at 1000 µg/ml (94.5%) followed by AgLeNp (91.5%) and AgPeNp (78%), ensuring the fruit as the richest source of antioxidants.

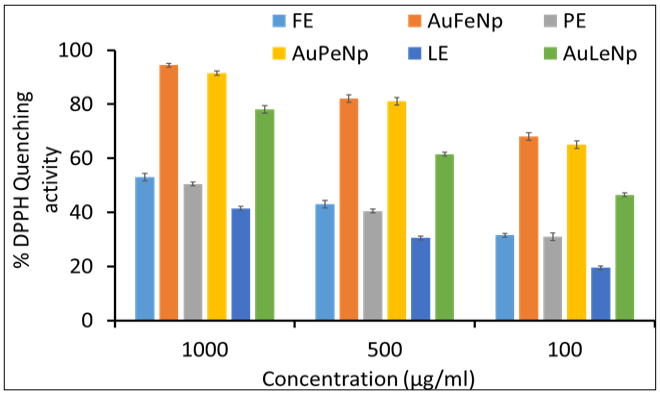

Fig 3.3: DPPH free-radical scavenging activity (%) of AuFeNps, AuLeNps, AuPeNps) along with their respective extracts (fruit (FE), leaf (LE) and peel (PE) extracts).

Though AuNp showed little less DPPH scavenging potency (dose dependent manner) than AuFeNp, but AuLeNp showed least activity (Fig 3.3). Even at 100 µg/ml, AuFeNp and AuPeNp showed 68% and 65% activity respectively. It was interesting to note that all the three AuNps made from fruit juice, peel and leaf extract showed greater antioxidant activity in comparison to their respective extracts. Literature suggests that AuNps when modified or capped by phytochemicals or polyphenols through green strategy, their antioxidant potential have been enhanced. This enhancement is attributed to the antioxidants present in the phytochemicals which can alter the surface chemistry of nanoparticles, subsequently enhancing the biological properties of Nps. The presence of the highest amounts of flavonoids, carotenoids, vitamin B1, B2, B12, and folic acid in fruit juice can be the reason behind high antioxidant potential. Whereas, peel consists of flavonones in the form of aglycones and glycosides, phenolic acids and Vitamin C.

3.4 Antimicrobial activity

To establish if the biosynthesized AuNps had the potential to combat the growth of deadly pathogens, Zone of inhibition (Kirby Bauer method) approach was followed where, growth of the pathogens on the agar plate was inhibited around the disc on which the nanoparticles were loaded, projecting a clear zone surrounding the disc. Zone ranged between 8 to 18 mm on a sterile disc of size 6 mm. According to Table No. 3.3, Fig 3.4 (A, B). AuFeNp is showing best antimicrobial potential against both Gram-positive (*B. cereus*) and Gram- negative (*P. aeruginosa*) microbes, followed by AuPeNp. Similar kind of pattern was observed when microbroth dilution assay was performed to find out the concentration at which AuNps were able to inhibit the growth of the pathogens (MIC). Considering Multidrug resistant– *Pseudomonas aeruginosa* as a deadly pathogen which needs immediate therapeutic alternative, it was interesting to find out that AuFeNp was able to kill it at a minimum concentration of ~10 µg/ml.

Table 3.3: Zone of inhibition exhibited by AuNps on pathogens

Zone of Inhibition (mm)			
Bacteria/AuNps	**AuFeNp**	**AuPeNp**	**AuLeNp**
B. cereus	17.5	14.5	11.5
P. aeruginosa	15.75	13.25	10
MDR- *P. aeruginosa*	13.5	12	8.5

Table 3.4: Minimum Inhibitory Concentration (MIC) of AuNps against pathogens

Minimum Inhibitory Concentration (µg/ml)			
Bacteria/AuNps	**AuFeNp**	**AuPeNp**	**AuLeNp**
B. cereus	7.5	11.5	27
P. aeruginosa	3.5	10.5	33.5
MDR- *P. aeruginosa*	9.5	16	57.5

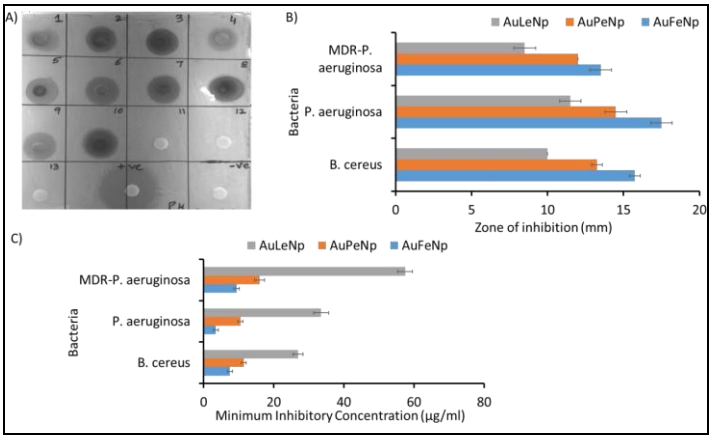

Fig 3.4: A) Zone of inhibition displayed by AuNps against MDR-PA, B) Graph showing respective zone of inhibition in mm, C) Minimum Inhibitory concentration of AuNps against Gram positive and Gram negative

The MIC of AuPeNp and AuLeNp followed AuFeNp, where AuLeNp showed highest concentration of ~58 µg/ml, which is around 6 times higher than AuFeNp (Fig 3.4C, Table 3.4). This concludes that AuLeNp also showed killing potency, but it was least among the Nps. The reason can be the larger size of the AuLeNp compared to AuFeNp and AuPeNp. Literature suggests that in various size preparations of nanoparticles, the smaller Nps shows enhanced toxicity in comparison to the larger size Nps at the same concentration. Reason for this can be the larger surface area of the smaller Nps. It provides rapid release of metal ions (Gold here), better interaction between cells and Nps along with high interactions with the solvent ions, so that more metal ions can be drawn from the Nps. Also, the phytochemicals bound on the surface of the Nps can have direct physical access to the cells as larger surface area is provided by nanoparticles, resulting in cumulative toxicity of the biosynthesized AuNps. For additional analysis of cell survival in a time-dependent approach, growth kinetics was performed for 12 hours, against MDR-PA at the respective MIC of AuNps along with considering untreated as control. It led to the growth curve of MDR-PA, which showed that AuFeNp had the best antibacterial potential (Fig 5A). When the survival percent was calculated at the MIC, it was found to be less than 1% growth (Fig 3.5B). The media of the MIC well was plated on an agar plate to analyze the number of live bacteria. As identified from Fig 5C, for all the three particles, AuFeNp, AuPeNp, and AuLeNp, none colonies were visible post 12 hours of incubation. These results indicate that cells could not recover until 12 hours of post treatment by AuNps when compared to the untreated, stating AuNps impose growth stress (thus inhibition) on MDR- PA.

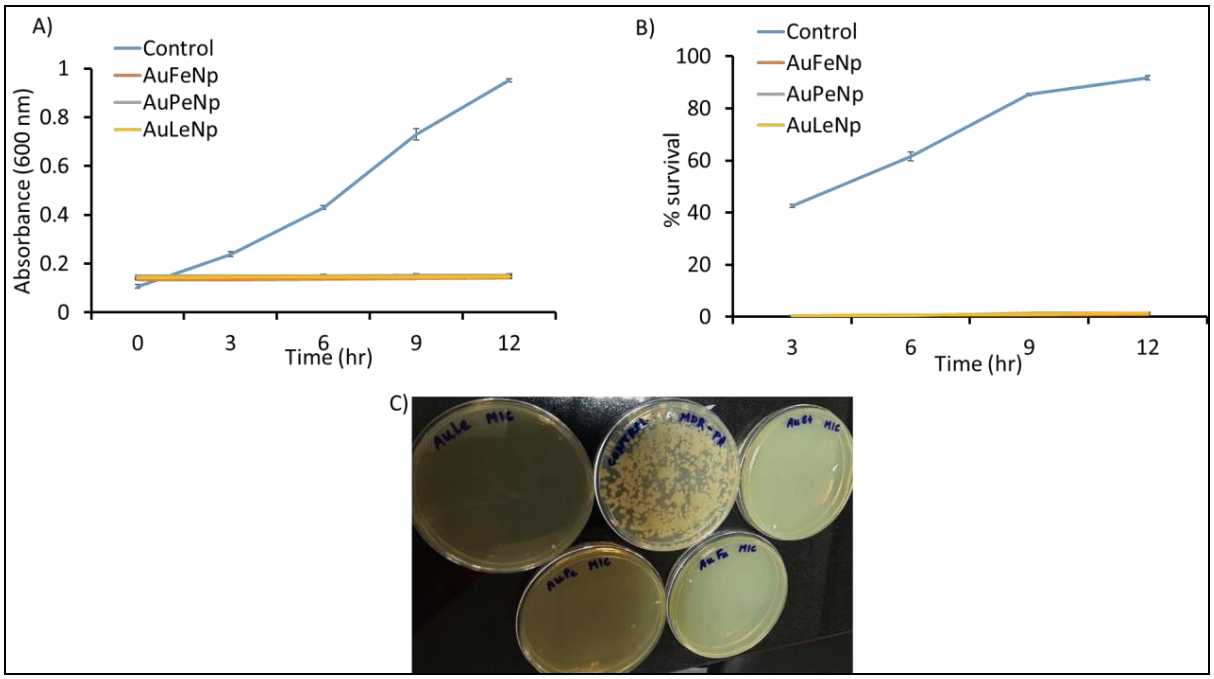

Fig 3.5: A) Time kinetics displaying growth of MDR- PA for 12 hr with and without treatment with AuNps, B) Survival percentage of MDR- PA post treatment with AuNps, C) Colony forming units of MDR- PA on agar plates after treating it at the respective MIC of AuNps

3.4.1 Mechanism of antimicrobial action

Since, AuFeNps showcased the best antibacterial activity against MDR- PA, when compared to AuPeNp and AuLeNp. Thus, AuFeNp was examined for its mechanism of antimicrobial potential against Gram-negative bacteria MDR- PA. Firstly, to analyze the morphological changes on treatment with AuFeNp, treated and untreated bacteria was observed through Transmission Electron Microscopy. As observed in Fig 3.6A, post 30 min (Fig 3.6A(b), the nanoparticles are seen to be attached on the cell membrane of the bacteria. After 60 min (Fig 3.6A(c)) of treatment, the cell membrane seems to be breaking due to the penetration of the AuFeNps. Considering Figure, post 90 min (Fig 3.6A(d), not only the cell membrane but the cell itself is seen to be ruptured as a whole, as compared to the untreated bacteria which served as control (Fig 3.6A(a)). TEM images declares that AuNps has pronounced antimicrobial potential and the mechanism of action lies through initial binding and later permeabilizing the cell membrane.

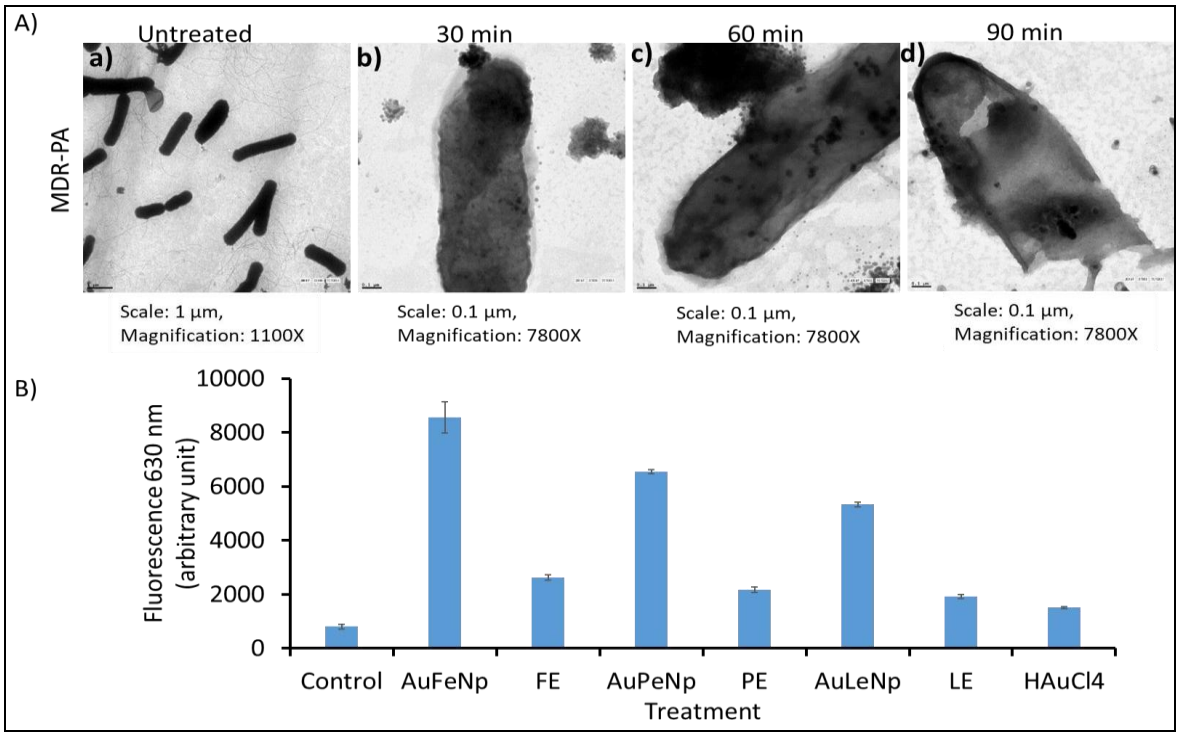

Fig 3.6: A) MDR-PA on treatment with AuNps shows aggregation of Nps on cell membrane and dismantling of the cell wall. B) Propidium iodide fluorescence in the cells demonstrates the cell permeability by AuNps

This was also established by treating the AuNps conditioned cells with a nucleic acid intercalating, cell impermeable dye, Propidium iodide (PI), which cannot stain live cells. Though it easily permeabilizes and stains the nucleic acid of dead cells. Fig 3.6B describes that AuFeNp showed highest PI permeability in MDR- PA cells followed by AuPeNp and AuLeNp. Fluorescence intensity generated by PI in AuFeNp treated cells was ~10 times higher than the untreated cells, and 4 times higher than the fruit extract (FE) treated MDR-PA, suggesting that AuNps were able to rupture the cell membrane in order to create toxicity, which was indicated perfectly by PI uptake by the dead cells. It claims the fact that in the gold nanoparticles form, the antimicrobial activity can be a cumulative effect of the phytochemicals adsorbed on the surface of the nanoparticles and the nano version of gold itself.

Cell permeability by AuNps was also demonstrated through the use of resazurin, a non-fluorescent dye. It is a non-permeable dye which gets converted to fluorescent resorufin through metabolism when resazurin interacts with the live cells. Given the Fig 7A below, the RFU is least for the AuFeNp treated MDR- PA when compared to AuPeNp, and AuLeNp, suggesting that least bacterial cells were alive to transfer electrons from NADPH + H^+ to resazurin (NADPH dehydrogenase), so as to reduce it to resorufin. The time kinetics (Fig 7B) done with the same dye, showed that minimum fluorescence was identified till 12 hours of incubation. Hence, till 12 hours, cells were not able to revive from the stress of AuNps treatment for growth, as compared to untreated cells which showed increase in fluorescence with time. This encourages to the point that AuNps can make the cell permeable and inhibits its further proliferation by entering into it.

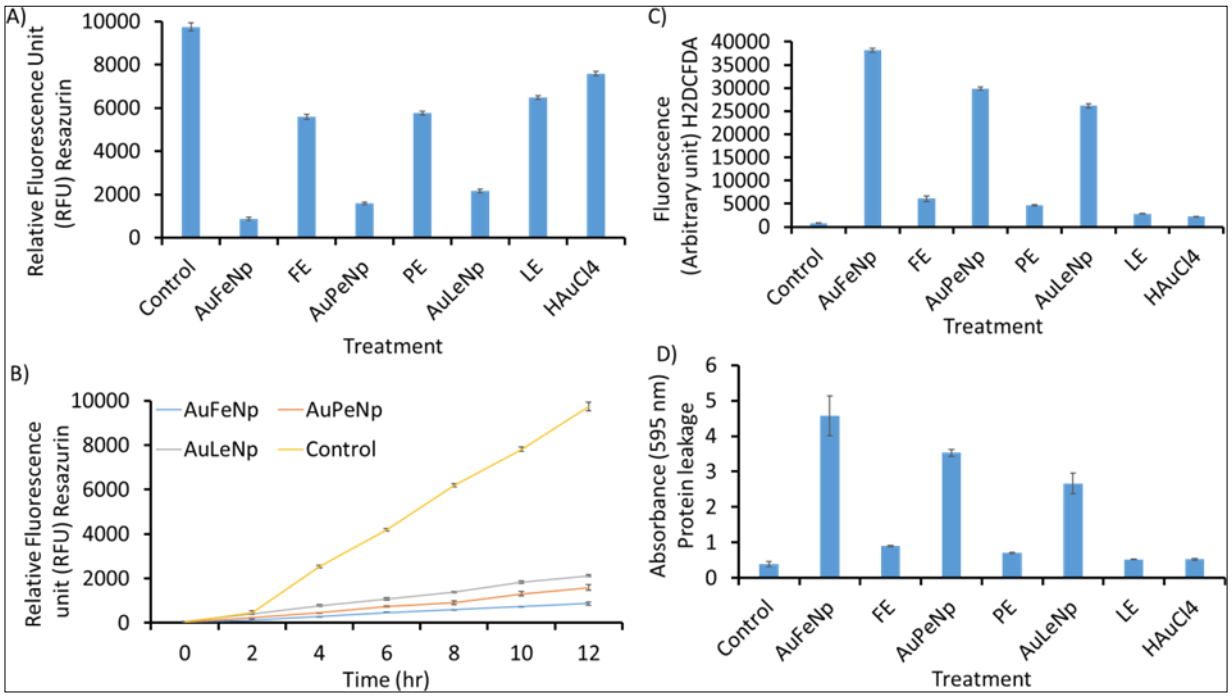

Fig 3.7: Deciphering the mechanism of action of antimicrobial potential of AuFeNps. A) Metabolic arrest in MDR- PA studied through Resazurin dye; B) Time kinetics of cell permeability; C) ROS generation in MDR- PA; D) Protein

By now it was established through TEM and cell permeability experiments that AuNps attach to the cell membrane and enter it to kill the bacterial cells. To identify what happens to the bacteria when AuNps enter the cells, an experiment was performed to see if AuNps can generate reactive oxygen species (ROS) on entering the cell. This was conducted using an oxidation-sensitive, cell permeant, dye, 2′,7′-dichlorodihydrofluorescein diacetate (H2DCFDA) to distinguish intracellular ROS status. Acetate groups get cleaved by intracellular esterases and oxidation, which converts the nonfluorescent H2DCFDA to highly fluorescent 2',7'-dichlorofluorescein. Fig 7C represents a high level of ROS in AuNps treated MDR- PA when compared to untreated or the cells treated with fruit, peel and leaf extracts. Enhanced fluorescence seen in AuNps treated cells, especially AuFeNp states high accumulation of ROS inside the cell. On the physiological front, ROS are generated as a natural answer to the usual metabolism of oxygen. But considering the mechanism of ROS generation by nanoparticles, it can be attributed to the release of metal ions (Gold metal in this case) in the cell through Fenton or Fenton like reaction, which multiplies the intracellular ROS. Nanoparticles are vehemently attracted to the cell membrane, where ROS can be generated and lipid peroxidation of outer membrane. The amended fatty acid composition of the cell membrane ascends cell permeability, leading to uncontrolled transport of nanoparticles into the cytoplasm from the extracellular environment. Nanoparticles once inside the cytoplasm induces another round of ROS bursts into the cell, leading to organelle rupture and leakage of cellular contents like nucleic acids and proteins, while damaging the cell totally. Increased ROS in the cell can damage the cell structure (distorted membrane), protein and DNA, thus influencing the functional machinery of the cell. This was clearly seen in this study that AuNps treated bacterial supernatant had more

protein content (Fig 3.7D). The reason behind this can be the damaged cell membrane and increased ROS inside the cell through AuNps treatment. ROS ambushes the hydrophobic residues of amino acids, breaking the peptide bonds thus, constraining the conformation and function of proteins. Oxidative damage also leads to the carbonylation of proteins, which thereby forms irreversible aggregates that cannot be deteriorated by proteasomes, hence permanently damaging the protein function.

Possessing antioxidant properties, Glutathione (GSH) can fortify the cell from toxicity of ROS along with influencing the redox facets of the intracellular environment. ROS converts GSH to GSSG (Glutathione disulfide) through oxidation. Oxidized glutathione is reduced by glutathione reductase incited by oxidative stress, the proportion of reduced and oxidized glutathione forms is the key regulating factor for cellular oxidative stress level. A decrease in the GSH level corresponds to increased oxidative stress. This pattern of GSH level is visible in the Fig. 3.8A, where AuFeNp is displaying the lowest GSH level, ~10 folds less than the control. When compared with the respective extracts, the nano formulated gold is showing higher depletion of GSH. This indicates that the action of generating oxidative stress in the bacterial system is a cumulative result of the phytochemicals present in the extract and the nano version of the gold ions secreted inside the cell. In the presence of AuNps, especially AuFeNps, cells are not able to recover well, as seen in the 12-hour kinetics study mentioned above. This can be attributed to the constant lowering of GSH (increased oxidative damage) in the cell, which directly affected the recovery and hence proliferation of this pathogen.

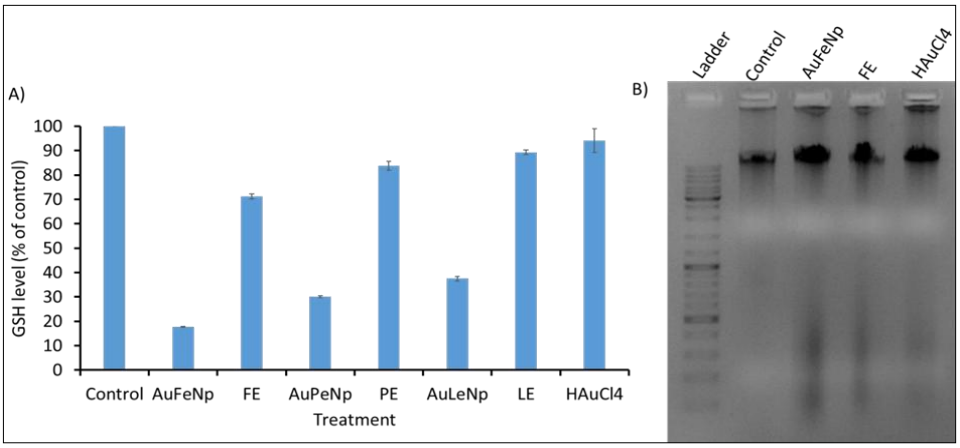

Fig 3.8: A) Depletion of GSH by AuNps in MDR- PA bacteria B) Genomic DNA damage shown in response to oxidative stress generated in the cell

DNA andNA (nucleic acids) are vital for cells to function, grow, and develop, but their nucleotide components are exposed targets of ROS. Because nanoparticles can induce ROS generation, significant single, double stranded breaks in DNA and chromosomal damage is observed by ROS. This was clearly seen in the Fig 3.8B, that when genomic DNA was isolated from AuFENp treated MDR-PA, major DNA fragmentation occurred, followed by DNA fragmentation induced by fruit extract and Gold chloride. Whereas, control genomic DNA remained intact as it was isolated from the untreated bacteria. AuNps mediated DNA damage can arrest the cell division, capacity to proliferate further and finally cell death.

3.4.2 Biocompatibility of nanoparticles in bacteria-keratinocyte co-culture model

In Figure 3.9A-C, it is clearly visible that there is less release of LDH in comparison to the Triton (positive control for LDH release). LDH release in the cell is directly correlated with the cell damage. The observations suggests that when the keratinocyte cells are infected with bacteria (MDR- PA) in the presence of AuFeNps in order to analyze the antimicrobial efficacy of Nps in a co-culture system, keratinocytes are not damaged in the process of killing the bacteria in the system. Thus, not only the cell viability of keratinocyte was less affected but, LDH release was observed less post AuFeNp treatment, stating the biocompatibility of the gold nanoparticles in a co-culture of bacteria and keratinocyte. This result conveys that pathogen mediated cytotoxicity is also avoided when gold nanoparticles are present in the co-culture system.

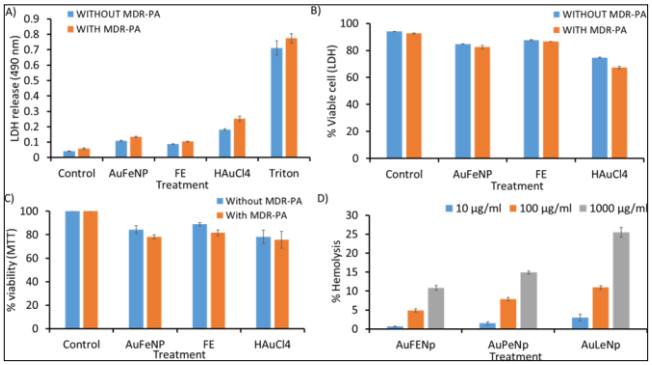

Fig 3.9: Biocompatibility assay of AuFeNps in bacterial-keratinocyte co-culture model. A) Release of LDH by keratinocytes in co-culture system B) Viability of AuNps treated keratinocytes in co-culture system estimated by LDH assay C) Viability of AuNps treated keratinocytes in co-culture system estimated by MTT assay D) Toxicity of AuNps on human Red Blood Cells

In order to identify whether keratinocytes can proliferate better when treated with AuNps, HaCaT (keratinocytes) were treated with AuFeNps for 24 hr and the morphological

sanity of the cells was analyzed using Phalloidin dye and proliferation was checked by DAPI. As DAPI is a common dye used to analyze the cell cycle status of the cell, it can easily identify the nucleic acid damage. Considering Fig. 3.10, the panel of AuFeNp clearly demonstrates that the nucleus is not damaged over AuFeNp along with the maintenance of the cytoskeletal structure of HaCaT cells. This observation is in synchrony of the minimal LDH release from the keratinocytes on treatment with AuFeNps that HaCaT can sustain and proliferate in the AuFeNp conditions.

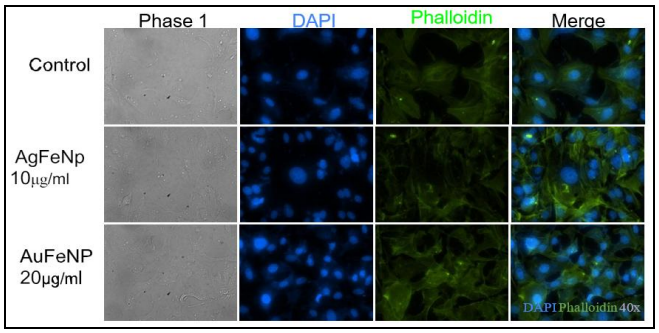

Fig 3.10: Morphological analysis of keratinocytes treated with nanoparticles

3.5 Anticancer potential of biosynthesized gold nanoparticles

Owing to the unique characteristics of rapid synthesis, biocatalytic and bioimaging efficiency, along with displaying therapeutic and drug delivery potential, Gold nanoparticles were also exploited for their role in inhibiting cancer cells *in vitro*. Various cancer cell lines, like breast cancer, melanoma and fibrosarcoma have been screened here in this study against AuNps. The pictorial analysis of the effect of the treatment of AuNps on cancer cell lines has been demonstrated in the Fig. 3.11 where the cells were imaged post 24 hours of treatment with AuNps. Efficacy was highly determined across all the cancer cell lines used here. Skin cancer melanoma cell line (B16-F10) was used further to analyze the mechanism of cell death due to AuNps and breast cancer cell lines were used further to find out cell migration capacity of cancer cells on treatment with AuNps. All the three AuNps, AuFeNp, AuPeNp and AuLeNp were screened for their anticancer role, though they displayed substantial activity, AuFeNps were used further for all the experimental analysis, as it consistently showed highest cancer cell inhibiting activity across the cell lines used in this study.

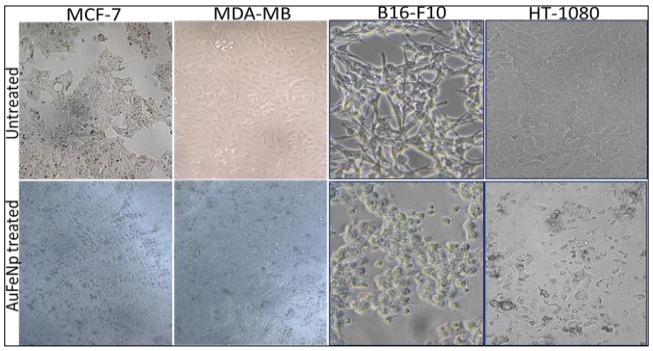

Fig 3.11: AuNps display cytotoxicity in various cancer cell lines

In order to quantify the toxicity of AuNps, trypan blue dye exclusion assay was carried out on B16-F10 cells and results were shown in Fig. 3.12A. After treating with AuNps the cells were visualized under inverted microscope and we detected stained cells (non-viable) with blue color and unstained cells (viable) without any color. As the viable cells didn't take up trypan blue due to their intact cell membrane, they were not stained and dead cells were stained because their cell membrane didn't have intact and functionalized membrane. Cell viability of all the cancer cell lines was identified through MTT assay and Cell titer glo assay. Both the assays represent the ATP metabolism capacity of the cells. The cell lines were treated with a series of concentrations from 1 to 100 ug/ml concentration in order to identify the exact concentration of inhibition of the cells. Fig B represents the percent survival at the concentration of 10 ug/ml, at this concentration less than 20% of cells were found viable. Similar kind of viability pattern was seen in breast cancer cells on treatment with AuFeNps. Though all the cells had cancer inhibiting capacity, AuFeNps is represented here due to the best anticancer potential. The cell permeabilization capacity of the AuFeNps was analyzed using Resazurin dye which also demonstrates the metabolic activity of the cells. Both the cancer cell lines are displaying metabolism arrest on treatment with AuFeNps.

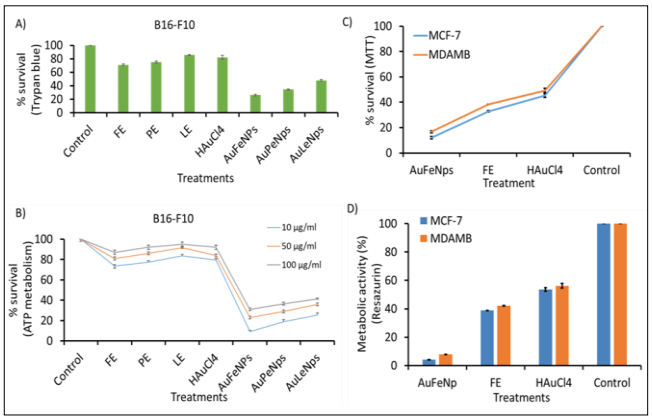

Fig 3.12: Anticancer potential displayed by AuNps on breast cancer and melanoma cell lines. A) Live/dead B16-F10 cancer cells analysis by Trypan blue dye B) Cytotoxicity of AuNps at various concentrations C) Cytotoxicity of AuNps on breast cancer cell lines D) Metabolic activity determination of cancer cell on treatment with AuFeNps

As per the above results, we confirmed that the biosynthesized AuNps are causing cytotoxicity to the mammalian cancer cell line. In order to investigate the cytotoxic effect of the biosynthesized nanoparticles, we have carried out different apoptosis detection methodologies on B16- F10 cell lines. B16- F10 cells were stained with AO/EtBr dye mixture after 48 hours of treatment with the biosynthesized AuFeNps (10 µg/ml- inhibitory concentration of cancer cells) to assess the apoptosis potential through morphological variations. The stained cells were examined under fluorescent microscope and we distinguished cells into different categories based on fluorescence emitted and morphological variations in the stained chromatin of nuclei, a) Viable cells with uniform bright green colored nuclei having well organized intact membrane structures,

b) Early apoptotic cells with slightly condensed chromatin as visible bright green granules or patches in the nuclei but still having intact membrane structures, c) Mid/Late apoptotic cell, which had highly condensed irregular fragmented chromatin with light red color, d) Uniform red fluorescence cells with light green colored corners indicating nonviable cells with normal nuclei. The differentially stained cells were represented in the Fig. 3.13A AuFeNps treated B16-F10 cells displayed highly condensed chromatin with membrane blabbing indicating the cell death has been triggered by inducing apoptosis. It also showed more mid/late apoptotic bodies with highly condensed nuclei. Drastic morphological changes in the nuclei of some B16-F10 cells were observed. Nanoparticles have been known to produce free radicals like hydroxyl, superoxide and hydrogen peroxide that cleaves DNA. According to the given Fig 3.13A (i), the green colored cells are healthy which have not reached apoptosis, but when compared to Fig 3.13A (iii) of the same, it clearly indicates early apoptotic cells as the nuclear part of the cells are orange in color, which is a sign of DNA damage and hence indicating the pathway of cell towards apoptosis. Based on our results we concluded that AuNps are causing apoptosis through chromatin condensation followed by Caspase-3 activation, finally leading to apoptosis of the cells. Since caspase-3 is a hallmark for programmed cell death or apoptosis, its expression identified in the Fig 3.13C, represents that cancer cells are killed by apoptosis, which is again linked to the chromosomal condensation seen in the B16-F10 AO/PI-stained cells.

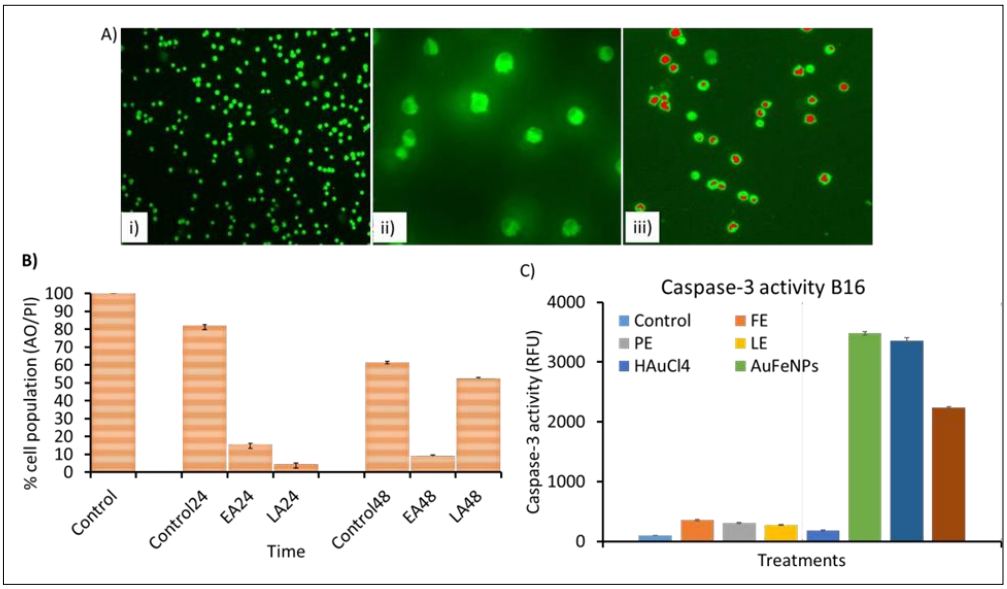

Fig 3.13: Characterization of apoptosis in B16-F10 murine melanoma cell line. A) Epifluorescence images of i) untreated B16-F10 cells, ii) Early apoptotic cells; 24 hours of AuFeNps treatment, iii) Late apoptotic cells; 48 hours of AuFeNps treatment B) Graph enumerating the cells reported to be early and late apoptosis C) Caspase-3 activation assayed to identify if mode of cell death of AuFeNps treated B16-F10 cells

3.6 Curbing the migration potential of the breast cancer cell line

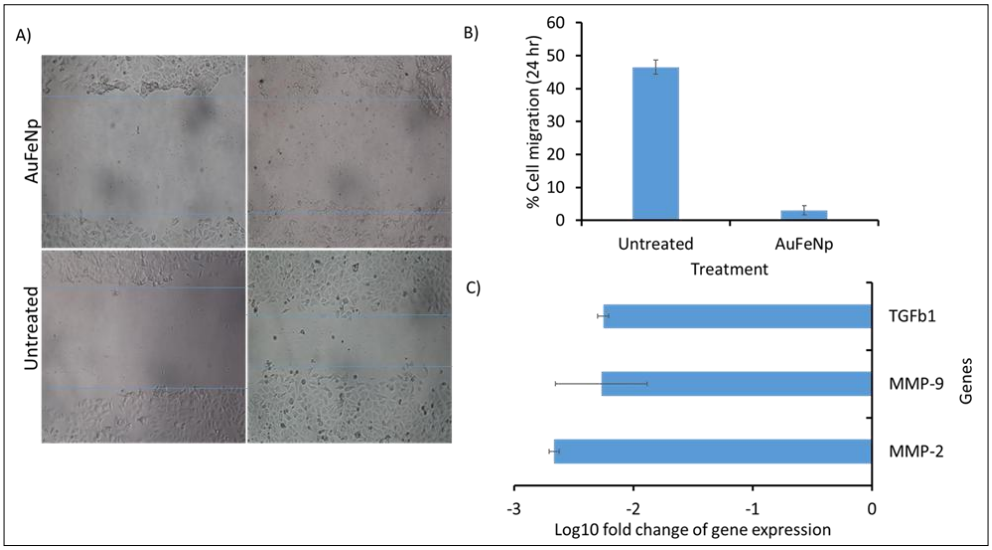

Fig 3.14: Inhibiting the migration capacity of breast cancer cells. A) Scratch assay showing the less migration potential of MCF-7 cells on AuFeNp treatment, B) % migration of cells shown in the graph, C) Expression of genes responsible for cell proliferation and migration

3.7 Cytotoxicity of biosynthesized gold nanoparticles on normal cell lines

To inspect the anti-metastatic assets of AuNps, a scratch wound assay was accomplished on breast cancer cell line, MCF-7. It was carried out to determine the migration potential of the cancer cells in order to heal the wound generated. AuFeNps exhibited inordinate inhibitory properties on cell migration as observed in the Fig 3.14A. When compared to the control where the cells could migrate from both the sides to reduce the wound (lessening of the wound area, represented by blue line), the cancer cells could not migrate so as to close the wound. The area where the cells had migrated from the initial day to the final day (24 hr later), was measured using ImageJ to identify the wound closure percentage. The observations indicate that AuNps has excellent potential to inhibit the migrating hence metastatic capacity of the breast cancer cells. This was also exemplified using the gene expression quantification of genes like MMP-2, MMP-9 and TGFb1. All the said three genes showed down regulation on treating the MCF-7 cells with AuFeNps. The extracellular matrix (ECM) is continuously remodeled by Matrix metalloproteinases (MMP), and the down regulation observed here suggests that the migrating and remodeling of wound cannot be sustained by the cancer cells when treated by AuFeNps.

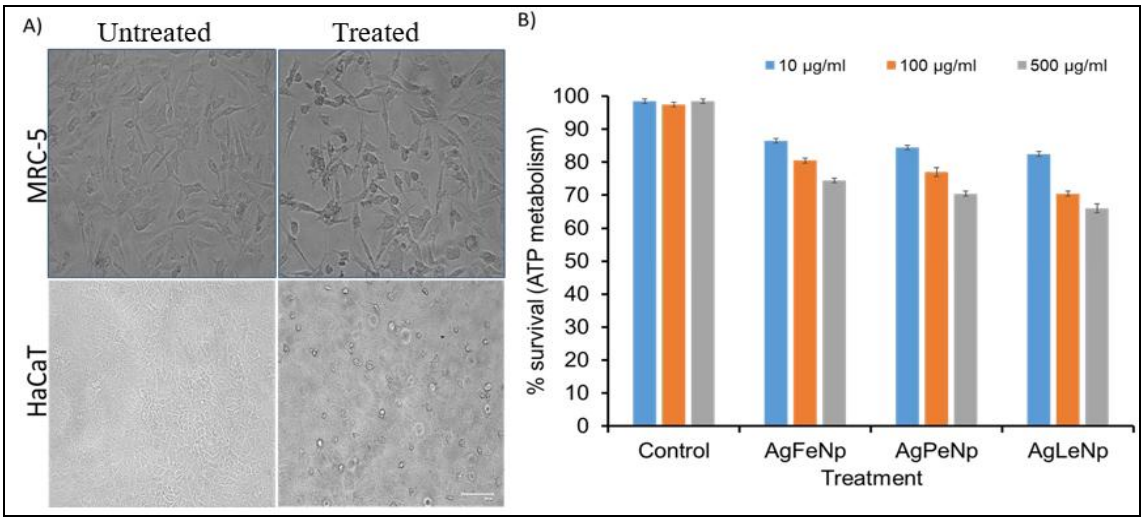

Fig 3.15: Toxicity profile of AuNps on normal cell lines. A) Fibroblasts (MRC-5) and Keratinocytes (HaCaT)

It is imperative for any nanomaterial or nano-formulation to have applications in terms of its role in inhibiting deadly antibiotic resistant pathogens or proliferation of uncontrolled cancer cells, but the most important factor that makes it useful and viable is its biocompatibility with the mammalian cells. In the Fig. 3.15A, treating both fibroblasts and keratinocytes (non-cancer cell lines) with AuNps, it was observed that there is nominal toxicity in them and they can proliferate in the presence of AuNps. When the survival condition of the fibroblasts was analyzed by MTT assay, the results suggested that fibroblasts can survive ~70% when treated with 50 times higher AuNp concentration (10 ug/ml is the concentration).

4. Conclusion

Conclusively, this study contributes to the exploitation of antibacterial, and anticancer potential of Gold nanoparticles synthesized from the fruit juice, leaf and peel extracts of the *Citrus maxima* plant. It demonstrated excellent bactericidal capacity against MDR-*Pseudomonas aeruginosa*. Not only antibacterial but AuNps could also inhibit the migration and proliferation of cancer cell lines in vitro. These particles can be further studied for their role in vivo and clinical prospects.

5. References

1. Sun X, Wang Y, Sha J. Development and application of giant magnetoresistance (GMR) biosensors. Journal of East China University of Science and Technology. 2026;52(2):151-167. doi:10.14135/j.cnki.1006-3080.20250513001.
2. Brown D, Manuel W, Luu D, Luong TD, Morales Vega M, Phan MH. High-precision detection of magnetic nanoparticles in microfluidic biosensing systems. Biosensors. 2026;16(5):291. doi:10.3390/bios16050291.
3. Chen M, Liu J, Zhang K, Song X, Tan X, Wang Q, Giesy JP, et al. Application of biomimetically synthesized magnetic nanoparticles to the improvement of biosensor detection in soils contaminated with metal(loid)s. Journal of Hazardous Materials. 2026;514:142663. doi:10.1016/j.jhazmat.2026.142663.
4. Zhang G, Liang P, Fu X, Wang Y. Precision intervention based on infection site: strategies and advances of magnetic nanomaterials in bacterial therapy. Frontiers in Chemistry. 2026;14:1794622. doi:10.3389/fchem.2026.1794622.
5. Wang Z, Wei L, Sun X, Zhao X. Magnetic sensing technologies: principles and recent advances in food safety analysis. Food Chemistry. 2026;523:150129. doi:10.1016/j.foodchem.2026.150129.
6. Sun H, Li J, Zhao C, Ren C, Tian T, Lei C, et al. A highly sensitive giant magnetoresistive (GMR) biosensor based on the magnetic flux concentrator effect. Micromachines. 2025;16(5):559. doi:10.3390/mi16050559.
7. Hwang KY, Brown D, Attanayake SB, Luu D, Nguyen MD, Lee TR, et al. Signal differentiation of moving

magnetic nanoparticles for enhanced biodetection and diagnostics. Biosensors. 2025;15(2):116. doi:10.3390/bios15020116.
8. Jagirani MS, Balouch A, Zhang T, Khuhawar AH, Hafsa U, Jagirani I, et al. Smart biosensing with magnetic nanoparticle-bioconjugates: recent advances and future trends: a review. Microchemical Journal. 2025:116228. doi:10.1016/j.microc.2025.116228.
9. Tripathy S, Ng KW, Sharma S, Vu NN, et al. A locked aptamer-magnetic nanoparticle assay for cardiac troponin I classification to support myocardial infarction diagnosis in resource-limited environments. Biosensors and Bioelectronics. 2025;286:117590. doi:10.1016/j.bios.2025.117590.
10. Wang J, Shen Y, Hao G, Tang X, Dai H, Zhang H, et al. A washing-less biosensor based on the dual functions of magnetic separation and signal output of magnetic nanoparticles for the rapid and visual detection of enrofloxacin. Analytica Chimica Acta. 2025;1352:343923. doi:10.1016/j.aca.2025.343923.
11. Sun F, Pang K, Yang K, Zheng L, Wang M, Wang Y, et al. Aptamer-conjugated magnetic nanoparticles integrated with SERS for multiplex Salmonella detection. Biosensors. 2025;15(7):464. doi:10.3390/bios15070464.
12. Phuangkaew T, Saipai S, Hoven VP, Na Nongkhai P. Magnetic nanoparticles stabilized by phosphorylcholine-containing polymer for label-free C-reactive protein detection. ACS Omega. 2025;10:10317-10326. doi:10.1021/acsomega.4c10064.
13. Kiani-Salmi N, Bahramian B, Abedi-Firoozjah R, Ebrahimi A, Khezerlou A, Tavassoli M, et al. Recent advances and trends in magnetic nanoparticle-assisted aptasensors for foodborne bacteria monitoring: applications, challenges, and updates. Food Chemistry: X. 2025;31:103156. doi:10.1016/j.fochx.2025.103156.
14. Meenakshi M, Bhaskar R, Kumar SKA, Kumar RS. A concise review on magnetic nanoparticles: their properties, types, synthetic methods, and current trending applications. Current Nanoscience. 2025;21(1):2-17. doi:10.2174/0115734137271993231109174718.
15. Singh V, Rana S, Rathaur P, Faizi FR, Singh A. Advancing biomedical innovations: a review of magnetic nanoparticles. Nanoscience & Nanotechnology-Asia. 2025;15(4). doi:10.2174/0122106812387110250714094126.
16. Chand, et al. Magnetic nanoparticles: synthesis and applications in life sciences. ChemistryOpen. 2025. doi:10.1002/open.202500214.
17. Radic J. Review of magnetic nanomaterials for the electrochemical sensing of antibiotics. ACS Applied Nano Materials. 2025. doi:10.1021/acsanm.5c03689.
18. Guo X, et al. Pollen-inspired magnetic nanoparticles with dual-recognition sensing interfaces for intelligent-response modulation of circulating tumor cells capture and release. Biosensors and Bioelectronics. 2025:117932. doi:10.1016/j.bios.2025.117932.
19. Integrated microfluidic giant magnetoresistance (GMR) biosensor platform for magnetoresistive immunoassay of myoglobin. Biosensors. 2025;16(1):8. doi:10.3390/bios16010008.
20. Construction of the indicator-free electrochemical biosensor with magnetically self-assembly based on Fe3O4/α-Fe2O3 magnetic heterogeneous nanorods for the ultra-sensitive detection of CYFRA 21-1 DNA. Frontiers in Chemistry. 2025;13:1696542. doi:10.3389/fchem.2025.1696542.
21. Wang M, Jin L, Leung PHM, Chow FWN, Zhao X, Chen H, et al. Advancements in magnetic nanoparticle-based biosensors for point-of-care testing. Frontiers in Bioengineering and Biotechnology. 2024;12:1393789. doi:10.3389/fbioe.2024.1393789.
22. Rezaei B, Yari P, Sanders SM, Wang H, Chugh VK, Liang S, et al. Magnetic nanoparticles: a review on synthesis, characterization, functionalization, and biomedical applications. Small. 2024;20(5):2304848. doi:10.1002/smll.202304848.
23. Hong J, Wang L, Zheng Q, Cai C, Yang X, Liao Z. The recent applications of magnetic nanoparticles in biomedical fields. Materials. 2024;17(12):2870. doi:10.3390/ma17122870.
24. Magnetic nanoparticles: synthesis, characterization, and their use in biomedical field. Applied Sciences. 2024;14(4):1623. doi:10.3390/app14041623.
25. Mishra S, Yadav MD. Magnetic nanoparticles: a comprehensive review from synthesis to biomedical frontiers. Langmuir. 2024;40(33):17239-17269. doi:10.1021/acs.langmuir.4c01532.
26. Çiçek Özkul SL, Kaba İ, Ozdemir Olgun FA. Unravelling the potential of magnetic nanoparticles: a comprehensive review of design and applications in analytical chemistry. Analytical Methods. 2024;16:3620-3640. doi:10.1039/D4AY00206G.
27. Behyar MB, Nilghaz A, Ebrahimi R, Hasanzadeh M, Shadjou N. Advancements in magnetic aptasensors: recent progress and future trends in biosensor technology. TrAC Trends in Analytical Chemistry. 2024;172:117549. doi:10.1016/j.trac.2024.117549.
28. Liang S, Wu K, Wang JP. Magnetoresistive (MR) biosensor. In: Magnetic Nanoparticles in Nanomedicine. Elsevier; 2024. p.289-322. doi:10.1016/B978-0-443-21668-8.00010-9.
29. Guo X, Hu F, Zhang Y, Zhao S, Wan Y, Wang B, et al. Magnetic nanoparticle-based microfluidic platform for automated enrichment of high-purity extracellular vesicles. Analytical Chemistry. 2024;96(18):7212-7219. doi:10.1021/acs.analchem.4c00795.
30. Xu Y, et al. CRISPR/Cas12a-driven electrochemiluminescence and fluorescence dual-mode magnetic biosensor for sensitive detection of Pseudomonas aeruginosa based on iridium(III) complex as luminophore. Biosensors and Bioelectronics. 2024;264:116678. doi:10.1016/j.bios.2024.116678.
31. Li T, Meng F, Fang Y, Luo Y, He Y, Dong Z, et al. Multienzymatic disintegration of DNA-scaffolded magnetic nanoparticle assembly for malarial mitochondrial DNA detection. Biosensors and Bioelectronics. 2024;246:115910. doi:10.1016/j.bios.2023.115910.
32. Detection of factor Xa activity using giant magnetoresistive biosensors. Analytica Chimica Acta. 2024;1331:343347. doi:10.1016/j.aca.2024.343347.
33. Reddy SM, Stephen AN, Holden MA, Stockburn WJ,

Dennison SR. Magnetic nanoparticle-facilitated rapid mass production of high affinity polymeric materials (nanoMIPs) for protein recognition and biosensing. Biomaterials Science. 2024;12(22):5845-5855. doi:10.1039/D4BM00990H.
34. Manavalan RK, Enoch K, Volegov AS, Angusamy G, Nallasivam S. Review on medical applications of manganese oxide (Mn2+, Mn3+, and Mn4+) magnetic nanoparticles. Journal of Nanomaterials. 2024:1073915. doi:10.1155/2024/1073915.
35. Ma X, Jiang P, Geng J, Li X, Jin Y, Li B, et al. Magnetic nanoparticle-decorated metal organic frameworks for chemiluminescence detection of glutathione. Microchimica Acta. 2024;191(10):618. doi:10.1007/s00604-024-06686-6.
36. Tan X, Huang D, Zhao M, et al. GMR detection of magnetic beads with different sizes. Journal of Magnetism and Magnetic Materials. 2024;597:171992. doi:10.1016/j.jmmm.2024.171992.
37. Comprehensive introspection of magnetoresistive sensors applied in biomedical diagnostics. Current Medical Imaging. 2024;20. doi:10.2174/1573405620666230825113444.
38. Magnetic nanoparticles and their applications. In: Nanomedicine. Wiley; 2024. doi:10.1002/9783527830404.ch9.
39. Cryogenically induced highly ordered single-strand DNA-modified magnetic nanoprobes for rapid and ultrasensitive bioanalysis. Analytical Chemistry. 2025;97(13):7260-7270. doi:10.1021/acs.analchem.4c06869.
40. A lateral flow biosensor based on isothermal amplification for visual identification of species and sex from bloodstain. Analytical Chemistry. 2024. doi:10.1021/acs.analchem.4c01623.
41. Wu K, Tonini D, Liang S, Saha R, Chugh VK, Wang JP. Giant magnetoresistance biosensors in biomedical applications. ACS Applied Materials & Interfaces. 2022;14(8):9945-9969. doi:10.1021/acsami.1c20141.
42. Mostufa S, Rezaei B, Yari P, Xu K, et al. Giant magnetoresistance based biosensors for cancer screening and detection. ACS Applied Bio Materials. 2023;6(10):4042-4059. doi:10.1021/acsabm.3c00592.
43. Su D, Wu K, Srinivasan K, et al. Ultra-flexible giant magnetoresistance biosensors for lab-on-a-needle biosensing. Advanced Materials Interfaces. 2023;10(7):2201417. doi:10.1002/admi.202201417.
44. Kim S, Wang SX, Lee JR. Real-time temperature correction for magnetoresistive biosensors integrated with temperature modulator. Biosensors and Bioelectronics: X. 2023;14:100356. doi:10.1016/j.biosx.2023.100356.
45. Carinelli S, Luis-Sunga M, González-Mora JL, Salazar-Carballo PÁ. Synthesis and modification of magnetic nanoparticles for biosensing and bioassay applications: a review. Chemosensors. 2023;11(10):533. doi:10.3390/chemosensors11100533.
46. Wang Y, Guan M, Hu C, Mi F, Geng P, Li Y. High-sensitivity biosensor based on SERS integrated with dendrimer-assisted boronic acid-functionalized magnetic nanoparticles for IL-6 detection in human serum. Nanotechnology. 2023;34(35). doi:10.1088/1361-6528/acceaa.
47. Huang H, Zhang Z, Li G. A review of magnetic nanoparticle-based surface-enhanced Raman scattering substrates for bioanalysis: morphology, function and detection application. Biosensors. 2023;13(1):30. doi:10.3390/bios13010030.
48. Recent approaches in magnetic nanoparticle-based biosensors of miRNA detection. Magnetochemistry. 2023;9(1):23. doi:10.3390/magnetochemistry9010023.
49. Yao C, Ng E, Wang SX. An automated and mobile magnetoresistive biosensor system for early hepatocellular carcinoma diagnosis. Biosensors and Bioelectronics. 2022;202:113982. doi:10.1016/j.bios.2022.113982.
50. Ravi N, Chang SE, Franco LM, et al. A GMR-based assay for quantification of the human response to influenza. Biosensors and Bioelectronics. 2022;205:114086. doi:10.1016/j.bios.2022.114086.